Low Mach Number Modeling of Type Ia Supernovae. II. Energy Evolution

A. S. Almgren[1], J. B. Bell[1], C. A. Rendleman[1], M. Zingale[2,3]

ABSTRACT

The convective period leading up to a Type Ia supernova (SN Ia) explosion is characterized by very low Mach number flows, requiring hydrodynamical methods well-suited to long-time integration. We continue the development of the low Mach number equation set for stellar scale flows by incorporating the effects of heat release due to external sources. Low Mach number hydrodynamics equations with a time-dependent background state are derived, and a numerical method based on the approximate projection formalism is presented. We demonstrate through validation with a fully compressible hydrodynamics code that this low Mach number model accurately captures the expansion of the stellar atmosphere as well as the local dynamics due to external heat sources. This algorithm provides the basis for an efficient simulation tool for studying the ignition of SNe Ia.

Subject headings: supernovae: general — white dwarfs — hydrodynamics — nuclear reactions, nucleosynthesis, abundances — convection — methods: numerical

1. Introduction

Modeling the period of convection leading up to the ignition of Type Ia supernovae (SNe Ia) is critical to determining the distribution of hot spots that seed the subsequent explosion. Multidimensional simulations of SNe Ia explosions presently seed one or more hot spots at or near the center of a white dwarf and use a flame model to describe the subsequent evolution (see for example Röpke & Hillebrandt 2005; Gamezo et al. 2005; Plewa et al. 2004). Variations in the size, number, and distribution of these seeds can lead to large

[1]Center for Computational Science and Engineering, Lawrence Berkeley National Laboratory, Berkeley, CA 94720

[2]Dept. of Astronomy & Astrophysics, The University of California, Santa Cruz, Santa Cruz, CA 95064

[3]Dept. of Physics & Astronomy, SUNY Stony Brook, Stony Brook, NY 11794-3800

differences in the explosion outcome (Niemeyer et al. 1996; García-Senz & Bravo 2005; Livne et al. 2005). The convective flows leading up to ignition have Mach numbers of 0.01 or less, with temperature perturbations of only a few percent (Woosley 2001; Woosley et al. 2004)—conditions that are extremely challenging for fully compressible codes. One-dimensional statistical methods (Wunsch & Woosley 2004) predict that off-center ignition is likely, but they cannot give information about the distribution of the hot spots. Only recently has progress been made in multidimensional modeling of convection in white dwarfs. The first such calculations (Höflich & Stein 2002) evolved a two-dimensional wedge of the star for a few hours using an implicit hydrodynamics algorithm. Convective velocities of approximately 100 km s^{-1} developed. They observed compression near the center of the star leading to slightly off-center ignition. Three-dimensional anelastic calculations (Kuhlen et al. 2006), showed a large-scale dipole flow dominating the evolution, leading to an off-center ignition. These simulations used a spectral decomposition, with a small portion of the center of the star removed due to the coordinate singularity at $r = 0$. Neither of these calculations operated at a Reynolds number large enough to see fully developed turbulence. Further three-dimensional studies are needed to see how robust this dipole flow is to rotation and convection at higher Reynolds and Rayleigh numbers.

The goal of the present work is the development of a new multidimensional hydrodynamics algorithm capable of evolving the full star from the convective phase, though ignition and into the early stages of flame propagation. Long time integration is critical. As we showed previously (Almgren et al. 2006—henceforth paper I), the low Mach number hydrodynamics equations provide an accurate description of flows with Mach numbers less than 0.2. By filtering out sound waves, the low Mach number approximation allows for much larger time steps ($\sim 1/M$ larger) than corresponding compressible codes. In contrast to the anelastic equation set, the low Mach number equations are capable of modeling flows with finite-amplitude density and temperature perturbations. The only restriction is that the pressure perturbation be small. Furthermore, because the compressibility effects due to both the background stratification and local heat release are included, the low Mach number equations set can self-consistently evolve the expansion of a hydrostatic atmosphere due to heat release (Almgren 2000).

In this paper, we continue the development of the low Mach number hydrodynamics algorithm to include the effects of heat release. An energy equation is added, and an earlier assumption from paper I is relaxed, now allowing the background state to vary in time. In § 2 we develop the low Mach number equation set. In § 3 the numerical methodology is explained. Comparisons to fully compressible calculations are provided in § 4 to demonstrate the accuracy and utility of our new algorithm. We conclude in § 5.

2. Low Mach Number Hydrodynamics

In paper I, we derived a system of low Mach number equations for stellar atmospheres for which there was a time-independent background state. The necessary assumption for validity of this system was that the Mach number (M) of the flow be small. In this case, any pressure deviations from the base state pressure, which are $O(M^2)$, are also small. The perturbations of density and temperature need not be small.

This system is valid for many low Mach number terrestrial and stellar flows, but fails to capture the correct atmospheric response to large-scale heating that radially shifts the entire atmosphere at and above the level at which the heating occurs. This was shown analytically for the terrestrial atmosphere, using the pseudo-incompressible approximation, in Bannon (1996). In Almgren (2000) it was shown that when time variation of the background state is correctly included, the solution calculated by the low Mach number equation set is identical to that reached by the fully compressible equation set.

Physically, this is consistent with the interpretation of the low Mach number equations as representing instantaneous acoustic equilibration. If heating of a local parcel of fluid results in a large temperature perturbation from the ambient, the effect of the resultant acoustic waves is to return the parcel to pressure equilibrium with the fluid around it by expansion of the parcel. The density and temperature variations of the parcel relative to the ambient values may be large, but the parcel will remain close to pressure equilibrium.

By contrast, when an entire layer of the atmosphere is heated, the acoustic equilibration process brings the entire layer to a new hydrostatic equilibrium. Consider a horizontally uniform atmosphere with heating uniformly applied throughout a horizontal layer. The response of the atmosphere will itself be horizontally uniform, and for positive heating each parcel of fluid above the heated layer will rise in its respective radial column. In equilibrium, given the assumption that no fluid is lost at the top boundary, then following an upward shift of each parcel, the mass of fluid above any given parcel will not have changed. If gravitational acceleration is effectively constant over the length scale of the base state displacement, then the weight of fluid above a parcel will not have changed. Thus for an atmosphere in hydrostatic equilibrium the pressure of each parcel will not have changed, although that parcel will have changed its radial location. In other words, the material derivative, rather than the time derivative, of the base state pressure must be zero. Numerical examples in § 4 of this paper will confirm the time-dependent response of the base state as well as of the full state is necessary to correctly capture the atmospheric response to large-scale heat release.

We note that the assumption of constant gravity over the displacement distance of the base state does not mean one must assume constant gravity over the full domain. In practice

the length scale of the base state adjustment is much smaller than the length scale of more localized motions.

We now generalize the low Mach number equation set from paper I to allow for time dependence of the base state. We recall from paper I the fully compressible equations of motion in a stellar environment, but here we add an external heat source, $H_{\rm ext}$, and again neglect compositional and reaction terms:

$$\begin{aligned} \frac{\partial \rho}{\partial t} + \nabla \cdot (\rho \mathbf{U}) &= 0 \ , \\ \frac{\partial (\rho \mathbf{U})}{\partial t} + \nabla \cdot (\rho \mathbf{U}\mathbf{U}) + \nabla p &= -\rho g \mathbf{e}_r \ , \qquad (1) \\ \frac{\partial (\rho E)}{\partial t} + \nabla \cdot (\rho \mathbf{U} E + p\mathbf{U}) &= \nabla \cdot (\kappa \nabla T) - \rho g (\mathbf{U} \cdot \mathbf{e}_r) + \rho H_{\rm ext} \ , \qquad (2) \end{aligned}$$

and an equation of state

$$p = p(\rho, T) \ .$$

Here ρ, $\mathbf{U}$, T, and p are the density, velocity, temperature and pressure, respectively, $E = e + \mathbf{U} \cdot \mathbf{U}/2$ is the total energy with e representing the internal energy, and $g(r)$ is the radially dependent gravitational acceleration (resulting from spherically symmetric self-gravity), $\mathbf{e}_r$ is the unit vector in the radial direction, and κ is the thermal conductivity. The Reynolds number of flows in a typical white dwarf is sufficiently large that we neglect viscosity here, though viscous terms could easily be included in the model and the numerical methodology.

Again we choose to work with enthalpy, $h = e + p/\rho$, rather than energy, replacing Eq. [2] above by

$$\frac{\partial (\rho h)}{\partial t} + \nabla \cdot (\mathbf{U} \rho h) = \frac{Dp}{Dt} + \rho H \ , \qquad (3)$$

where $\rho H = \rho H_{\rm ext} + \nabla \cdot (\kappa \nabla T)$ represents the enthalpy source terms, and $D/Dt = \partial t + \mathbf{U} \cdot \nabla$ represents the Lagrangian (or material) derivative. (For the purposes of this paper we could alternatively use the entropy equation,

$$\rho T \frac{DS}{Dt} = \rho H \ ,$$

but for future work in which the source terms due to reactions are essential we will prefer the enthalpy formulation.)

We recall from the low Mach number asymptotics in paper I that the assumption that $M = |\mathbf{U}|/c \ll 1$ is sufficient to decompose the pressure into a base state pressure, p_0, and a perturbational pressure, π, i.e.

$$p(\mathbf{x}, r, t) = p_0(r, t) + \pi(\mathbf{x}, r, t) \ ,$$

where $\pi/p_0 = O(M^2)$. Here $\mathbf{x}$ represents the horizontal coordinate directions and r represents the radial direction. We define the base state density, ρ_0, by assuming hydrostatic equilibrium of the base state; this allows us to rewrite Eq. [1] in the form

$$\frac{\partial(\rho\mathbf{U})}{\partial t} + \nabla\cdot(\rho\mathbf{U}\mathbf{U}) + \nabla\pi = -(\rho-\rho_0)g\mathbf{e}_r$$

with no loss of generality.

Continuing to follow the derivations of paper I but with a time-dependent base state, we rewrite conservation of mass as an expression for the divergence of velocity:

$$\nabla\cdot\mathbf{U} = -\frac{1}{\rho}\frac{D\rho}{Dt} \quad . \tag{4}$$

Differentiating the equation of state, $p = p(\rho, T)$, along particle paths, we can write

$$\frac{D\rho}{Dt} = \frac{1}{p_\rho}\left(\frac{Dp}{Dt} - p_T\frac{DT}{Dt}\right) \quad , \tag{5}$$

with $p_\rho = \partial p/\partial\rho\big|_T$, and $p_T = \partial p/\partial T\big|_\rho$.

An expression for DT/Dt can be found by applying the chain rule to the enthalpy equation (Eq. [3]):

$$\frac{DT}{Dt} = \frac{1}{\rho c_p}\left((1-\rho h_p)\frac{Dp}{Dt} + \rho H\right) \quad , \tag{6}$$

where $c_p = \partial h/\partial T\big|_p$ is the specific heat at constant pressure, and $h_p = \partial h/\partial p\big|_T$ for convenience. Substituting Eq. [6] into Eq. [5] and the resulting expression into Eq. [4] yields

$$\nabla\cdot\mathbf{U} = \frac{1}{\rho p_\rho}\left(\frac{p_T}{\rho c_p}(1-\rho h_p) - 1\right)\frac{Dp}{Dt} + \frac{1}{\rho p_\rho}\left(\frac{\rho p_T H}{\rho c_p}\right) \quad ,$$

still with no loss of generality. Now, replacing p by $p_0(r,t)$ and recalling the definition of H, we write the divergence constraint as

$$\nabla\cdot\mathbf{U} + \alpha\left(\frac{\partial p_0}{\partial t} + \mathbf{U}\cdot\nabla p_0\right) = \frac{1}{\rho p_\rho}\left(\frac{p_T}{\rho c_p}\left(\nabla\cdot(\kappa\nabla T) + \rho H_{\rm ext}\right)\right) \equiv \tilde{S} \quad ,$$

where

$$\alpha(\rho, T) \equiv -\left(\frac{(1-\rho h_p)p_T - \rho c_p}{\rho^2 c_p p_\rho}\right) = \frac{1}{\Gamma_1 p_0} \quad ,$$

and $\Gamma_1 \equiv d(\log p)/d(\log\rho)\big|_s$. We recall from paper I that $\nabla\cdot\mathbf{U} + \alpha\mathbf{U}\cdot\nabla p_0$ can be rewritten as $1/\beta_0\nabla\cdot(\beta_0\mathbf{U})$ where

$$\beta_0(r,t) = \beta(0,t)\exp\left(\int_0^r \frac{1}{(\Gamma_1 p)_0}\frac{\partial p_0'}{\partial r}\,dr'\right) \quad . \tag{7}$$

Thus we can write the constraint as

$$\nabla \cdot (\beta_0 \mathbf{U}) = \beta_0 (\tilde{S} - \alpha \frac{\partial p_0}{\partial t}) \ . \tag{8}$$

For the purposes of comparing the fundamental hydrodynamic behavior of this low Mach number model to the established compressible formulation, we will from now on neglect thermal conduction. Summarizing the low Mach number equation set for this specialized case, with the momentum equation re-written as an evolution equation for velocity, we have

$$\begin{aligned} \frac{\partial \rho}{\partial t} &= -\nabla \cdot (\rho \mathbf{U}) \ , \\ \frac{\partial (\rho h)}{\partial t} &= -\nabla \cdot (\rho \mathbf{U} h) + \frac{D p_0}{D t} + \rho H_{\rm ext} \ , \qquad (9) \\ \frac{\partial \mathbf{U}}{\partial t} &= -\mathbf{U} \cdot \nabla \mathbf{U} - \frac{1}{\rho} \nabla \pi - \frac{(\rho - \rho_0)}{\rho} g \mathbf{e}_r \ , \\ \nabla \cdot (\beta_0 \mathbf{U}) &= \beta_0 \left(\sigma H_{\rm ext} - \frac{1}{\Gamma_1 p_0} \frac{\partial p_0}{\partial t} \right) \ , \qquad (10) \end{aligned}$$

where we define, for convenience, $\sigma = p_T/(\rho c_p p_\rho)$.

This system differs from that in paper I in that now p_0 and ρ_0 are unknowns as well as ρ, ρh, $\mathbf{U}$, and π. The equation of state was used to derive the constraint thus to include it here would be redundant. When reactions and compositional effects are included in future work, evolution equations for species will be added to this system and reaction terms will be added to the enthalpy equation and divergence constraint, but for the hydrodynamical tests we present here this system is sufficient.

We follow the approach used in Almgren (2000) to compute the time evolution of the base state, recalling from the beginning of this section that the pressure of each parcel remains unchanged during base state adjustment, i.e.,

$$\frac{D p_0}{D t} = 0 \ . \tag{11}$$

We first calculate the radial velocity field, denoted w_0, that adjusts the base state. We decompose the full velocity field, $\mathbf{U}$, into $w_0 \mathbf{e}_r$ and the remaining velocity field, $\widetilde{\mathbf{U}}$, that governs the more local dynamics, i.e.,

$$\mathbf{U}(\mathbf{x}, r, t) = w_0(r, t) \ \mathbf{e}_r + \widetilde{\mathbf{U}}(\mathbf{x}, r, t) \ , \tag{12}$$

and write Eq. [10] in terms of w_0 and $\widetilde{\mathbf{U}}$,

$$\nabla \cdot (\beta_0 w_0 \mathbf{e}_r) + \nabla \cdot (\beta_0 \tilde{\mathbf{U}}) = \beta_0 \left(\sigma H_{\rm ext} - \frac{1}{\Gamma_1 p_0} \frac{\partial p_0}{\partial t} \right) \ . \tag{13}$$

We then integrate Eq. [13] over a horizontal slab $\Omega_H \times (r-h, r+h)$ to obtain

$$\int_{r-h}^{r+h} \int_{\Omega_H} \left(\nabla \cdot (\beta_0 w_0 \mathbf{e}_r) + \nabla \cdot (\beta_0 \tilde{\mathbf{U}}) \right) dr \; d\mathbf{x} = \int_{r-h}^{r+h} \int_{\Omega_H} \beta_0 \left(\sigma H_{\rm ext} - \frac{1}{\Gamma_1 p_0} \frac{\partial p_0}{\partial t} \right) dr \; d\mathbf{x}, \tag{14}$$

Assuming solid wall or periodic boundary conditions on the horizontal boundaries, or that the horizontal velocity decays sufficiently as we reach the horizontal boundaries, we can simplify the volume integrals into area integrals over Ω_H,

$$\int_{\Omega_H} \left((\beta_0 w_0) + (\beta_0 \tilde{\mathbf{U}}) \cdot \mathbf{e}_r \right) d\mathbf{x} \Big|_{r-h}^{r+h} \;=\; \int_{r-h}^{r+h} \int_{\Omega_H} \beta_0 \left(\sigma H_{\rm ext} - \frac{1}{\Gamma_1 p_0} \frac{\partial p_0}{\partial t} \right) dr \; d\mathbf{x}, \tag{15}$$

To define the model we want to partition the velocity field so that the horizontal average of the radial flux due to heating be entirely incorporated into w_0 rather than $\widetilde{\mathbf{U}}$, namely

$$\int_{\Omega_H} \widetilde{\mathbf{U}} \cdot \mathbf{e}_r \; d\mathbf{x} \equiv 0 \;\; ,$$

Using this relationship, and taking the limit as $h \to 0$ Eq. [15] can be simplified to

$$\frac{\partial (\beta_0 w_0)}{\partial r} \;=\; \beta_0 \left((\overline{\sigma H}) - \frac{1}{\Gamma_1 p_0} \frac{\partial p_0}{\partial t} \right) \;\; . \tag{16}$$

where we define $\overline{\sigma H} = 1/\text{Area}(\Omega_H) \int_{\Omega_H} (\sigma H_{\rm ext}) \; d\mathbf{x}$.

We can further simplify Eq. [16] by expanding $\partial(\beta_0 w_0)/\partial r = \beta_0 \partial w_0/\partial r + w_0 \partial \beta_0/\partial r$, exploiting $Dp_0/Dt = \partial p_0/\partial t + w_0 \partial p_0/\partial r = 0$ to replace $\partial p_0/\partial t$, and recalling from the definition of β_0 that $(1/\beta_0) \; \partial \beta_0/\partial r = (1/\Gamma_1 p_0) \; \partial p_0/\partial r$ (see Appendix B of paper I for the derivation of β_0.) Then

$$\frac{\partial w_0}{\partial r} = \overline{\sigma H} \;\; .$$

This system can be integrated by noting that if there exists a lower boundary at $r = r_0$ with zero normal velocity (such as the center of a star), then at any time, t,

$$w_0(r,t) = \int_{r_0}^{r} \overline{\sigma H}(r',t) \; dr' \;\; . \tag{17}$$

The base state pressure and density update follow from Eq. [11] and conservation of mass, respectively:

$$\frac{\partial p_0}{\partial t} \;=\; -w_0 \frac{\partial p_0}{\partial r} \tag{18}$$

$$\frac{\partial \rho_0}{\partial t} \;=\; -\frac{\partial (\rho_0 w_0)}{\partial r} \;\; . \tag{19}$$

There are now two choices for defining the new base state enthalpy; these options are analytically equivalent but may differ numerically. The first is to use the equation of state: $(\rho h)_0 = \rho_0 h(p_0, \rho_0)$. The second is to use Eq. [9]. In this second approach, we can exploit $Dp_0/Dt = 0$, but must also correctly partition the heating term in the right hand side of Eq. [9]. The partitioning is given by the requirement that the base state continue to satisfy the equation of state. Then, given $Dp_0/Dt = 0$,

$$\begin{aligned} \frac{Dh_0}{Dt} &= \left.\frac{\partial h_0}{\partial T}\right|_p \frac{DT_0}{Dt} = c_p(-\frac{p_\rho}{p_T})\frac{D\rho_0}{Dt} = \frac{\rho_0 c_p p_\rho}{p_T}\overline{\sigma H} \\ &= \frac{1}{\sigma_0}\overline{\sigma H} \ , \end{aligned}$$

recalling $\sigma = p_T/(\rho c_p p_\rho)$ and letting $\sigma_0 = \sigma(p_0, \rho_0)$. Returning to conservation form, we can write

$$\frac{\partial(\rho h)_0}{\partial t} = -\frac{\partial(w_0(\rho h)_0)}{\partial r} + \frac{\rho_0}{\sigma_0}\,\overline{\sigma H} \ . \tag{20}$$

Using the velocity decomposition (Eq. [12]) we can re-write the evolution equations for ρ and ρh as

$$\frac{\partial \rho}{\partial t} = -\nabla\cdot(\rho\widetilde{\mathbf{U}}) - \frac{\partial(\rho w_0)}{\partial r} \tag{21}$$

$$\frac{\partial(\rho h)}{\partial t} = -\nabla\cdot(\rho h\widetilde{\mathbf{U}}) - \frac{\partial(\rho h w_0)}{\partial r} + \tilde{w}\frac{\partial p_0}{\partial r} + \rho H_{\rm ext} \ , \tag{22}$$

where $\tilde{w} = \widetilde{\mathbf{U}}\cdot\mathbf{e}_r$. We can also write these in perturbational form (with no loss of generality):

$$\begin{aligned} \frac{\partial \rho'}{\partial t} &= -\nabla\cdot(\rho'(\widetilde{\mathbf{U}} + w_0\mathbf{e}_r)) - \nabla\cdot(\rho_0\widetilde{\mathbf{U}}) \\ \frac{\partial(\rho h)'}{\partial t} &= -\nabla\cdot((\rho h)'(\widetilde{\mathbf{U}} + w_0\mathbf{e}_r)) - \nabla\cdot((\rho h)_0\widetilde{\mathbf{U}}) + \tilde{w}\frac{\partial p_0}{\partial r} + \left(\rho H_{\rm ext} - \frac{\rho_0}{\sigma_0}\overline{\sigma H}\right) \ , \end{aligned}$$

using Eq. [19] and Eq. [20], where $\rho' \equiv \rho - \rho_0$ and $(\rho h)' \equiv (\rho h) - (\rho h)_0$.

The evolution of the velocity field becomes

$$\frac{\partial\widetilde{\mathbf{U}}}{\partial t} = -\widetilde{\mathbf{U}}\cdot\nabla\widetilde{\mathbf{U}} - w_0\frac{\partial\widetilde{\mathbf{U}}}{\partial r} - \tilde{w}\frac{\partial w_0}{\partial r}\mathbf{e}_r - \frac{1}{\rho}\nabla\pi - \frac{(\rho-\rho_0)}{\rho}g\mathbf{e}_r \ , \tag{23}$$

and subtracting Eq. [16] from Eq. [10], the constraint equation for $\widetilde{\mathbf{U}}$ becomes

$$\nabla\cdot(\beta_0\widetilde{\mathbf{U}}) = \beta_0(\sigma H)' \ . \tag{24}$$

where we define $(\sigma H)' = \sigma H_{\rm ext} - (\overline{\sigma H})$.

In summary, then, the evolution of the base state is described by Eq. [18] and Eq. [19], with w_0 given by Eq. [17], and the evolution of the full state is given by Eq. [21], Eq. [22] and Eq. [23] with the divergence constraint given by Eq. [24].

3. Numerical Methodology

Our strategy for evolving the low Mach number system with a time-varying base state is a fractional step approach. In each time step we first update density and enthalpy as if the base state were time-independent, giving us predicted values that can be used to construct time-centered values in the right hand side of Eq. [17]. We then compute the evolution of the base state and recompute the updates to density and enthalpy, incorporating the base state adjustment. Finally, we update and project the velocity field to define the new values of velocity and pressure. The upwind methodology used to update all the state variables provides a robust discretization of the convective terms that avoids any stability restriction other than the CFL constraint, i.e. the time step scales linearly with the grid spacing and inversely with the maximum magnitude of the velocity in any one coordinate direction in the domain.

All base state quantities as well as all state quantities other than the perturbational pressure, π, are defined at cell centers and integer time levels. The perturbational pressure is defined at nodes and at half-times; similarly, the advective velocity and fluxes used for advective updates are defined at edges and half-times. In this section we replace $\widetilde{\mathbf{U}}$ by $\mathbf{U}$ for convenience of notation.

Initialization Specification of the initial value problem includes initial values for p_0, ρ_0 and h_0 (or T_0) as well as U, ρ and h (or T) at time $t = 0$, and a description of the boundary conditions, but the perturbational pressure is not initially prescribed. We calculate β_0 at $t = 0$ using Eq. [7]. Given this initial β_0, we project the initial velocity field to ensure that it satisfies the divergence constraint at $t = 0$. Then initial iterations of the following steps (typically two are sufficient) are performed to calculate an approximation to the perturbational pressure at $t = \Delta t/2$. At the end of each initial iteration all variables other than π are reset to their initial values.

The following steps are components of the single time step taken to advance the solution from t^n to t^{n+1}.

Step 1 In this step we construct $\mathbf{U}^{\mathrm{ADV}}$, a time-centered, second-order accurate, staggered-grid approximation to $\mathbf{U}$ at $t^{n+1/2}$, using an unsplit second-order Godunov procedure (Colella 1990). To do so we first predict $\mathbf{U}^{\mathrm{ADV},*}$ using the cell-centered data at t^n and the lagged pressure gradient from the interval centered at $t^{n-1/2}$. The provisional field, $\mathbf{U}^{\mathrm{ADV},*}$, represents a normal velocity on cell edges analogous to a MAC-type staggered grid discretization of the Navier-Stokes equations (Harlow & Welch 1965). However, $\mathbf{U}^{\mathrm{ADV},*}$ fails to satisfy the time-

centered divergence constraint (Eq. [24]). We apply a discrete projection by solving the elliptic equation

$$D^{\rm MAC}(\frac{\beta_0^n}{\rho^n}G^{\rm MAC}\phi^{\rm MAC}) = D^{\rm MAC}(\beta_0^n\mathbf{U}^{\rm ADV,*}) - \beta_0^n\left((\sigma H)'\right)^n$$

for $\phi^{\rm MAC}$, where $D^{\rm MAC}$ represents a centered approximation to a cell-based divergence from edge-based velocities, and $G^{\rm MAC}$ represents a centered approximation to edge-based gradients from cell-centered data. The solution, $\phi^{\rm MAC}$, is then used to define

$$\mathbf{U}^{\rm ADV} = \mathbf{U}^{\rm ADV,*} - \frac{1}{\rho^n}G^{\rm MAC}\phi^{\rm MAC} \quad .$$

In the above equations, we average β_0^n and ρ_0^n from centers to edges, i.e., ${\beta_0}_{j+1/2}^n = 1/2({\beta_0}_j^n + {\beta_0}_{j+1}^n)$, $\rho_{i+1/2,j}^n = 1/2(\rho_{i,j}^n + \rho_{i+1,j}^n)$ and $\rho_{i,j+1/2}^n = 1/2(\rho_{i,j}^n + \rho_{i,j+1}^n)$.

Step 2 We update ρ and ρh as if $w_0 = 0$ and the base state were constant, i.e., we discretize

$$\begin{aligned}
\frac{\partial\rho}{\partial t} &= -\nabla\cdot(\rho'\mathbf{U}) - \nabla\cdot(\rho_0\mathbf{U}) \quad , \\
\frac{\partial(\rho h)}{\partial t} &= -\nabla\cdot((\rho h)'\mathbf{U}) - \nabla\cdot((\rho h)_0\mathbf{U}) + w\frac{\partial p_0}{\partial r} + \rho H_{\rm ext}
\end{aligned}$$

using the second-order advection methodology as in paper I with $\rho H_{\rm ext}$ treated as an explicit source term. The discretization takes the form

$$\begin{aligned}
\rho^{n+1,*} &= \rho^n - \Delta t\left[\nabla\cdot(\rho'\mathbf{U}^{\rm ADV})\right]^{n+1/2} - \Delta t\nabla\cdot(\rho_0^n\mathbf{U}^{\rm ADV}) \quad , \\
(\rho h)^{n+1,*} &= (\rho h)^n - \Delta t\left[\nabla\cdot((\rho h)'\mathbf{U}^{\rm ADV})\right]^{n+1/2} - \Delta t\nabla\cdot((\rho h)_0{}^n\mathbf{U}^{\rm ADV}) \\
&\quad + \Delta t\; w^{\rm ADV}\left(\frac{\partial p_0}{\partial r}\right)^n + \Delta t\left(\rho H_{\rm ext}\right)^{n+1/2} \quad ,
\end{aligned}$$

where $w^{\rm ADV} = \mathbf{U}^{\rm ADV}\cdot\mathbf{e}_r$ and $\rho^{n+1/2} = 1/2(\rho^n + \rho^{n+1,*})$ in the construction of $\left(\rho H_{\rm ext}\right)^{n+1/2}$. The details of the upwind construction of $\left[\nabla\cdot(\mathbf{U}^{\rm ADV}\rho')\right]^{n+1/2}$ and $\left[\nabla\cdot(\mathbf{U}^{\rm ADV}(\rho h)')\right]^{n+1/2}$ are given in Appendix A, where we consider the construction of $\left[\nabla\cdot(\mathbf{V}s)\right]^{n+1/2}$ for any edge-based vector field $\mathbf{V}$ and cell-centered quantity s. In this step $\mathbf{V} = \mathbf{U}^{\rm ADV}$. The terms, $\nabla\cdot(\rho_0^n\mathbf{U}^{\rm ADV})$ and $\nabla\cdot((\rho h)_0^n\mathbf{U}^{\rm ADV})$, are defined differently, in that we do not upwind ρ_0 or $(\rho h)_0$ in this step, rather they are simply averaged onto edges as β_0 and ρ^n were averaged in **Step 1**.

Step 3 We integrate Eq. [17] to determine w_0 on edges,

$$w_{0j+1/2} = w_{0j-1/2} + \Delta r(\overline{\sigma H})_j^{n+1/2} \quad ,$$

using the equation of state given $\rho^{n+1/2}$ and p_0 to compute σ. We then update the base state quantities,

$$\begin{aligned}
(p_0)_j^{n+1} &= (p_0)_j^n - \frac{\Delta t}{2\Delta r}(w_{0j+1/2} + w_{0j-1/2})(p_{0\,j+1/2}^{n+1/2} - p_{0\,j-1/2}^{n+1/2}) \ , \\
(\rho_0)_j^{n+1} &= (\rho_0)_j^n - \frac{\Delta t}{\Delta r}((\rho_0 w_0)_{j+1/2}^{n+1/2} - (\rho_0 w_0)_{j-1/2}^{n+1/2}) \ , \\
(\rho h)_0^{n+1} &= \rho_0^{n+1}\ h(p_0^{n+1}, \rho_0^{n+1}) \ .
\end{aligned}$$

The construction of $p_{0\,j+1/2}^{n+1/2}$ and $\rho_{0\,j+1/2}^{n+1/2}$ is described in Appendix A. After construction of the new base state we compute β_0^{n+1} using Eq. [7], then set $\beta_0^{n+1/2} = 1/2(\beta_0^n + \beta_0^{n+1})$. We use the equation of state here to calculate $(\rho h)_0^{n+1}$ in order to keep the base state thermodynamically consistent.

Step 4 In this step we repeat the update of ρ and ρh, but in the prediction of the edge states here $\mathbf{V} = \mathbf{U}^{\rm ADV} + w_0\mathbf{e}_r$. We also center the $w\ \partial p_0/\partial r$ term in time:

$$\begin{aligned}
\rho^{n+1} &= \rho_0^{n+1} + (\rho^n - \rho_0^n) - \Delta t\left[\nabla\cdot(\rho'(\mathbf{U}^{\rm ADV} + w_0\mathbf{e}_r))\right]^{n+1/2} - \Delta t\nabla\cdot(\rho_0^n\mathbf{U}^{\rm ADV}) \\
(\rho h)^{n+1} &= (\rho h)_0^{n+1} + ((\rho h)^n - (\rho h)_0^n) - \Delta t\left[\nabla\cdot((\rho h)'(\mathbf{U}^{\rm ADV} + w_0\mathbf{e}_r))\right]^{n+1/2} \\
&\quad -\Delta t\nabla\cdot((\rho h)_0^n\mathbf{U}^{\rm ADV}) \\
&\quad +\frac{\Delta t}{2}\ w^{\rm ADV}\left(\left(\frac{\partial p_0}{\partial r}\right)^{n+1} + \left(\frac{\partial p_0}{\partial r}\right)^{n}\right) + \left(\rho H_{\rm ext} - \frac{\rho_0}{\sigma_0}\overline{\sigma H}\right)^{n+1/2} \ .
\end{aligned}$$

We use the perturbational form of these equations in order to ensure that numerically, if, as in the anelastic case, $\beta_0 \equiv \rho_0$, and $\rho^n = \rho_0^n$ and H is horizontally uniform, then $\rho^{n+1} = \rho_0^{n+1}$, i.e. no perturbation to the base state density is introduced in a case where analytically there should be none.

Step 5 We then update the velocity field, $\mathbf{U}^n$ to $\mathbf{U}^{n+1,*}$ by discretizing Eq. [23],

$$\begin{aligned}
\mathbf{U}^{n+1,*} &= \mathbf{U}^n - \Delta t\left[((\mathbf{U}^{\rm ADV} + w_0\mathbf{e}_r)\cdot\nabla)\mathbf{U}\right]^{n+1/2} - \Delta t w^{\rm ADV}\left(\frac{\partial w_0^{n+1/2}}{\partial r}\right)\mathbf{e}_r \\
&\quad -\frac{\Delta t}{\rho^{n+1/2}}\mathbf{G}\pi^{n-1/2} - \Delta t\frac{(\rho^{n+1/2} - \rho_0^{n+1/2})}{\rho^{n+1/2}}g\mathbf{e}_r \ ,
\end{aligned}$$

with $\rho^{n+1/2} = 1/2(\rho^n + \rho^{n+1})$ and $\mathbf{G}$ a discretization of the gradient operator. The construction of $\left[((\mathbf{U}^{\rm ADV} + w_0\mathbf{e}_r)\cdot\nabla)\mathbf{U}\right]^{n+1/2}$ is described in Appendix A with $\mathbf{V} = \mathbf{U}^{\rm ADV} + w_0\mathbf{e}_r$ and s set to each component of $\mathbf{U}^n$ individually. Finally, we impose the constraint (Eq. [24])

$$\nabla\cdot(\beta_0^{n+1/2}\mathbf{U}^{n+1}) = \beta_0^{n+1/2}\left((\sigma H)'\right)^{n+1}$$

by solving

$$L_\beta^\rho \phi = D\left(\beta_0^{n+1/2}\left(\frac{\mathbf{U}^{n+1,*}}{\Delta t} + \frac{1}{\rho^{n+1/2}}\mathbf{G}\pi^{n-1/2}\right)\right) - \frac{\beta_0^{n+1/2}\left((\sigma H)'\right)^{n+1}}{\Delta t}$$

for nodal values of ϕ where L_β^ρ is the standard bilinear finite element approximation to $\nabla \cdot (\beta_0/\rho)\nabla$ with ρ and β_0 evaluated at $t^{n+1/2}$. (See Almgren et al. (1996) for a detailed discussion of this approximate projection; see Almgren et al. (2000) for a discussion of this particular form of the projection operand.) We determine the new-time velocity field from

$$\mathbf{U}^{n+1} = \mathbf{U}^{n+1,*} - \frac{\Delta t}{\rho^{n+1/2}}\left(\mathbf{G}\phi - \mathbf{G}\pi^{n-1/2}\right) \quad ,$$

and the new time-centered perturbational pressure from

$$\pi^{n+1/2} = \phi \quad .$$

4. Numerical Results

We consider three numerical tests in this section, each studying the response of the atmosphere to prescribed external heating. For each test case, the initial conditions in the computational domain are specified in two parts. The lower portion of the domain is initialized with a one-dimensional hydrostatic white dwarf model up until the outer boundary of the white dwarf. This initialization is identical for the compressible and low Mach number models. The model is created by specifying a base density of 2.6×10^9 g cm^{-3} and base temperature of 7×10^8 K and integrating the equation of hydrostatic equilibrium outward while constraining the model to be isentropic. The composition is held constant at 0.3 ^{12}C and 0.7 ^{16}O, and the gravitational acceleration is fixed at -1.5×10^{10} cm s^{-2}. We use the stellar equation of state developed by Timmes & Swesty (2000). This procedure provides a reasonable approximation of the state of the white dwarf just before runaway. None of the methods described here require constant gravity, but it was assumed for simplicity in the comparisons.

The upper portion of the domain represents the region beyond the outer boundary of the white dwarf, and different approximations are used there for the compressible and low Mach number models. For the compressible calculations, the integration proceeds radially outward until the density reaches a threshold value of 10^{-4} g cm^{-3}. Throughout the integration we set a low temperature cutoff of 10^7 K, to keep the temperature in the outer layers of the model reasonable. Once the density drops below its cutoff, the integration is stopped and the material above it is held at constant density and temperature. This buffer region is necessary

to allow for expansion of the star; otherwise, as the star expands the loss of mass through the upper domain boundary would change the base pressure (Glasner et al. 2005), impacting the dynamics throughout the domain. Finally, for the multidimensional test cases, we add a convectively stable layer below the atmosphere to prevent any motions generated from the heating from interfering with the lower boundary. Figure 1 shows the initial temperature, density, entropy, and adiabatic indices (Γ_1 and $\gamma_e \equiv p/(\rho e) + 1$) as a function of height for the compressible background.

For the low Mach number model applied to the second and third test cases, the density cutoff is set to 2.5×10^6 g cm^{-3}, approximately the value at which the temperature cutoff is applied for the compressible background. Once the density reaches this cutoff the density, temperature and pressure are held constant, equivalent to gravity being set to zero radially outward of that position. Because the base state density in the buffer region is significantly higher for the low Mach number calculations than for the compressible calculations, this buffer region serves to damp motions that reach it without impacting the hydrostatic equilibrium of regions toward the center. Since the time step for the entire calculation is determined by the largest velocity in the domain, this damping is essential for low Mach number calculations in order to avoid excessively large velocities above the cutoff that would dictate an excessively small time step. An additional approximation in the outer region is that we set $\beta_0 \equiv \rho_0$ for $\rho_0 < 5 \times 10^7$ g cm^{-3} in order to suppress spurious wave formation at the outer boundary of the star.

In the first test, a layer of the star is heated for 5.0 s with a heating profile,

$$H = H_0 \exp(-(r - r_0)^2/W^2) \ ,$$

with $r_0 = 4 \times 10^7$ cm, $W = 10^7$ cm, and $H_0 = 1 \times 10^{17}$ erg g^{-1} s^{-1}. This energy generation rate is quite a bit higher than we would expect during the smoldering phase of the convection leading up to an SN Ia (Woosley et al. 2004), but necessary to see a response with the compressible code on a reasonable timescale. It also provides a more stringent test of the hydrostatic adjustment than a lower energy generation rate would give. Because the initial conditions and the heating are both one-dimensional, we use a reduced one-dimensional form of the equations to solve the systems. We contrast three different systems of equations.

For this one-dimensional test, we compare the low Mach number results to those produced by the fully compressible PPM method (Colella & Woodward 1984), as implemented in the FLASH code. Two versions of the low Mach number algorithm are used for this test. The first is the low Mach number equation set with time-varying base state (as described in § 2). The second is a formulation of the low Mach number equations in which the base state is time-independent (equivalent to the equation set present in paper I).

Figure 2 shows the density, temperature and pressure for the three solutions at $t = 5$ s. All simulations were run on a uniform grid with 768 zones spanning 2.5×10^8cm. The compressible and low Mach number expanding background solutions show excellent agreement. In the region of heating, the temperature has increased enormously, with a corresponding density decrease. The amplitude of the density decrease is much smaller, due to the degenerate nature of the equation of state. The inset in the density plot shows the density adjustment on a linear scale, showing the decrease at the heating height and an increase in the density above this. Both equation sets reach the same solution in response to the heating. The differences above 1.7×10^8 cm are due to the different treatments of the upper boundary, and are not significant to the atmospheric dynamics. As a result of the energy deposition, the model expands by almost 10^7 cm, or about 5%. In contrast, when the background is not allowed to adjust (dashed line), the low Mach number model fails to capture the expansion. While the temperature increases in the region of the heating, there is no expansion in the material above the heating layer. This is consistent with the point made in Bannon (1996) that the pseudo-incompressible equation set does not give the correct solution in the terrestrial atmosphere when the base state is not allowed to vary in time, and the demonstration in Almgren (2000) that the correct solution is found when the base state does absorb the horizontally averaged heating.

Figure 3 shows the difference in density before and after heating. Here we see more clearly the adjustment of the density structure as a result of the localized heating. There is a slight rise in the density in the compressible solution below the heated layer. This small error is due to the difficulty in constructing a lower hydrostatic boundary that allows sound waves to leave the domain. For the low Mach number case, the state remains unchanged below the heating layer, as it should. The compressible and expanding background low Mach number solutions show a large increase in the density above the heating layer. This is not present in the low Mach number case where the background was not allowed to expand.

In even this one-dimensional simulation, the choice of boundary conditions at the top and bottom boundaries of the computational domain is critical for the compressible calculations. The fully compressible code generates sound waves as it struggles to keep the hydrostatic solution steady on the grid. The boundary conditions must allow these disturbances to leave the domain or they will corrupt the solution. We use a hydrostatic lower boundary, integrating the pressure and density in the ghost cells using a fourth-order reconstruction of the pressure (Zingale et al. 2002), where the temperature is kept constant in the ghost cells and the velocities are given a zero gradient. This provides pressure support to the material while allowing sound waves to leave the domain. Further robustness is obtained by computing the hydrostatic structure in the boundary from the initial base density and temperature, and keeping this structure fixed in time. At the upper boundary, we set the

density and temperature to our cutoff values and allow the fluid to move out of the domain (with a zero gradient) but set inward velocities to zero. This has the effect of keeping the fluid velocities in this region small, and therefore, they do not dictate the time step.

The low Mach number calculations, by contrast, are not sensitive to mass exiting the top boundary, as the hydrostatic equilibrium is incorporated into the base state, which is independent of the total mass. A simple outflow boundary condition is used at the top (with any inflowing velocities set to zero), and a reflecting boundary condition is used at the bottom boundary. Additionally, the compressible calculations need to resolve the scale height of the atmosphere very well to suppress any ambient velocities generated by slight imbalances of the pressure gradient and gravitational force (see Zingale et al. 2002 for a discussion of this). This is not the case with the low Mach number method, so we expect our low Mach number solutions to numerically converge at a lower resolution than the compressible solutions.

For the second and third tests, we consider fully two-dimensional heating profiles, in which both parts of the new low Mach number algorithm are fully exercised. For these cases we compare the new low Mach number formulations with the compressible solution. In addition to the PPM algorithm, these multidimensional tests are also run with an unsplit compressible algorithm (Colella 1990), adapted to a general EOS, and incorporated into the FLASH framework. This is the same implementation of the unsplit method we described in paper I. The computational domain for these tests is 2.5×10^8cm by 3.5×10^8cm, spanned by a uniform grid with 640$\times$ 896 zones. Periodic boundary conditions are used on the sides of the domain.

In the second test, we specify three local regions of heating, designed to mimic "hot spots," but no heated layer as in the first case. In this scenario, while both the horizontal average and the local deviations from the horizontal average are non-zero, the deviations are much larger than the average, so the dominant effect is the local rather than horizontally averaged atmospheric response to the heating. For the first two seconds the heating profile has the form

$$H = H_0 \left\{ \sum_{i=1}^{3} \frac{a_i}{2} \left(1 + \tanh(2 - d_i/\sigma_i)\right) \right\} \tag{25}$$

where $d_i = \sqrt{(x - x_i)^2 + (r - r_i)^2}$ and the amplitudes, a_i, locations, (x_i, r_i), and widths, σ_i, of the perturbations are given in Table 1. After the first two seconds H is set to zero, and we continue to follow the evolution until $t = 4$ s. Figure 4 shows a time sequence from $t = 1$ to $t = 4$ s of temperature contours in a subset of the domain spanning from 5×10^7cm to 1.4×10^8cm high. The temperature is an independent variable in the compressible calculations, but in the low Mach number model, for these examples, we evolve density and compute temperature from the equation of state using density and p_0.

At early times, the three methods agree very well; at later times they diverge slightly. The vertical speed of the bubbles appears greatest with the low Mach number methodology followed by the unsplit compressible formulation; the PPM generates the slowest bubbles. We note that the difference in height between the PPM and unsplit methods is comparable to the difference between the unsplit and the low Mach number bubble heights. The precise reason for these differences is not yet completely understood; however, they serve to underscore the sensitivity of these flows and the difficulties in simulating them accurately with either the compressible or low Mach number approach.

Figure 5 shows a resolution study of this second test case for each of the three methods. The general trend one observes is that the location of the bubble rises with increased resolution. However, we also notice that the low Mach number model appears to converge to a solution at a lower resolution than either of the compressible models. This is likely due to the fact that hydrostatic equilibrium is guaranteed in the low Mach number method by the base state, while the compressible methods need considerable resolution just to keep the background medium quiescent. We also notice the difficulty that the PPM method has at the higher resolution, evidenced by the strong oscillations in temperature. This was also observed and discussed in paper I.

In the third test, we add the heated layer of the first test case to the three "hot spots" of the second case, resulting in a case for which the horizontal average of the heating is larger than the perturbation from the average. The heating profile has the form

$$H = H_0 \left\{ \exp(-(r - r_0)^2/W^2) + \sum_{i=1}^{3} \frac{a_i}{2}(1 + \tanh(2 - d_i/\sigma_i)) \right\} \tag{26}$$

where $r_0 = 7.5 \times 10^7$ cm and the amplitudes, a_i, locations, (x_i, r_i), and widths, σ_i, of the perturbations are as in the previous case and are given in Table 1. We apply the heating source for 2 s. As in the one-dimensional uniform heating case, we place the heating layer a bit above the lower boundary, so as to minimize contamination of the solution from lower boundary effects. Figure 6 shows the temperature contours for the unsplit compressible and low Mach number solver at $t = 1.5$ s, $t = 1.75$ s and $t = 2$ s. We again notice excellent agreement between the low Mach number and compressible results. We do not expect the exact shape of the rising bubbles to match precisely given the extremely unstable nature of the bubble's surface, but there is overall agreement between methods. Once again the low Mach number bubble rises slightly faster. We do not show the PPM results here, as the noise resulting from the dimensional splitting dominates the solution. We also note that at the final time, the low Mach number result shows a disturbance in the upper left corner of the domain. This disturbance is a result of a spurious wave generated at the outer boundary, which is not present in the compressible results because of the different treatment of the

outer boundary condition. The question of how best to represent the outer boundary of the white dwarf in a low Mach number calculation is still an open research question; at this point we note that while the high-velocity disturbance does restrict the time step, it does not appear to impact the solution in the primary region of interest. We also expect that more realistic heating profiles in three-dimensional geometries will not generate the disturbances in the outer boundary that we have observed in this final test case.

Figure 7 shows the horizontal average of the difference between density at $t = 2$s and $t = 0$s for the low Mach number and unsplit compressible results shown in Figure 6. On the left of this plot we see that the compressible solution has an increase in density over time below the level of the applied heating; this was also present in the first test case, although to a lesser degree. This error results from the difficulty in prescribing an accurate hydrostatic lower boundary. We note, however, that this is less than a 0.1% relative error in the density at this boundary. At approximately the center of the heated layer (7.5×10^7 cm) each calculation shows a negative average density variation. The small difference here between the compressible and low Mach number results here may also be a product of the lower boundary condition. Overall, however, the two algorithms agree well in the average response of the atmosphere to the heating.

Finally, since computational efficiency as well as accuracy is necessary for successful long-time integration, we comment on the relative efficiency of the low Mach number algorithm. For the second test case, for example, to evolve the state to 4.0 s, the unsplit compressible method took 14272 time steps while the low Mach number algorithm took only 233 time steps. For the final test case, evolving the solution to 1.5 s took 6532 timesteps for the unsplit method and 749 time steps for the low Mach number algorithm. Already by this point in the calculation, the spurious disturbance at the outer boundary of the star in the low Mach number algorithm is impacting the time step, decreasing the relative advantage of the low Mach number algorithm. As noted above, we expect this not to be the case for more realistic ignition scenarios. However, this case points out that to achieve the gains in efficiency possible with a low Mach number model one must successfully address this issue.

5. Conclusions

We have introduced a new algorithm for evolving low Mach number flows in the presence of local and large-scale heating. By contrast with the previous low Mach number model, this new model allows time variation of the base state in order to account for atmospheric expansion due to large-scale heat sources. The time evolution of the base state must be calculated at each time step in addition to the local dynamics. Numerical comparisons of low

Mach number simulations with simulations using a fully compressible code demonstrate that the low Mach number algorithm with a time-dependent base state can accurately capture the hydrostatic adjustment of an atmosphere as well as local dynamics in response to large- and small-scale heat release.

Our long-term goal is to develop the capability for full star simulation using the new low Mach number approach. The fundamental low Mach number approach has been validated with a number of simplified test cases, but further development is necessary to begin to perform detailed physics investigations of ignition and other problems of interest. This development will include extension to three dimensions with adaptive griding, radial representation of gravity and the base state within the three-dimensional setting, non-constant gravity, and the calculation of internal heating due to reaction networks.

The tests presented above are quite demanding, and provided a challenge to both the low Mach number and the compressible solvers. The energy generation and resulting temperature/density contrasts during the convective phase of an SN Ia are much smaller. Based on the agreement demonstrated on these difficult tests, we are confident that the low Mach number hydrodynamics method will be a useful and efficient tool in exploring the problem of SNe Ia ignition. In addition, this algorithm is applicable to a wide range of problems outside of our target application (SNe Ia), including Type I X-ray bursts, classical novae, and convection in stars.

We especially thank Stan Woosley for numerous discussions and interactions. We thank Jonathan Dursi for helpful comments on this paper. The compressible calculations presented here used portions of the FLASH Code (version 2.5), developed in part by the DOE-supported ASC/Alliance Center for Astrophysical Thermonuclear Flashes at the University of Chicago. Some calculations made use of resources of the National Energy Research Scientific Computing Center, which is supported by the Office of Science of the U.S. Department of Energy under Contract No. DE-AC02-05CH11231. This work was supported by the Applied Mathematics Program of the DOE Office of Mathematics, Information, and Computational Sciences under the U.S. Department of Energy under contract No. DE-AC02-05CH11231, by DOE grant No. DE-FC02-01ER41176 to the Supernova Science Center/UCSC, and by the NASA Theory Program (NAGW-5-12036/NNG05GG08G).

A. Construction of Advective Updates

Consider the construction of an advective update in the form $[\nabla \cdot (s\mathbf{V})]^{n+1/2}$, given the cell-centered velocity field $\mathbf{U}^n = (u, v)$, an edge-based velocity field, $\mathbf{V} = (\mathrm{V}^x, \mathrm{V}^r)$ and a

cell-centered scalar, s. For simplicity we will present the construction in two dimensions, although extension to three dimensions is straightforward and is given in detail in (Almgren et al. 1998).

We first extrapolate s from cell centers at t^n to edges at $t^{n+1/2}$ using a second-order Taylor series expansion in space and time. The time derivative is replaced using the evolution equation for s. If, for example, $s_t = -\nabla \cdot (s\mathbf{V}) = -\mathbf{V} \cdot \nabla s - s\nabla \cdot \mathbf{V}$, then

$$\begin{aligned} \tilde{s}^L_{i+1/2,j} &\approx s_{i,j} + \frac{\Delta \mathbf{x}}{2} s_x + \frac{\Delta t}{2} s_t \\ &= s_{i,j} + (\frac{\Delta \mathbf{x}}{2} - u_{i,j}\frac{\Delta t}{2})(s^{\lim}_x)_{i,j} + \frac{\Delta t}{2}(-(\widehat{vs_r})_{i,j} - s_{i,j}(\mathrm{V}^x_x + \mathrm{V}^r_r)_{i,j} \end{aligned}$$

extrapolated from (i, j), and

$$\begin{aligned} \tilde{s}^R_{i+1/2,j} &\approx s_{i+1,j} - \frac{\Delta \mathbf{x}}{2} s_x + \frac{\Delta t}{2} s_t \\ &= s_{i+1,j} + (-\frac{\Delta \mathbf{x}}{2} - u_{i+1,j}\frac{\Delta t}{2})(s^{\lim}_x)_{i+1,j} + \frac{\Delta t}{2}(-(\widehat{vs_r})_{i+1,j} - s_{i+1,j}(\mathrm{V}^x_x + \mathrm{V}^r_r)_{i+1,j} \end{aligned}$$

extrapolated from $(i+1, j)$. In evaluating these terms the first derivatives normal to the face (in this case $s^{\lim}_x$) are evaluated using a monotonicity-limited fourth-order slope approximation (Colella 1985). The construction of the transverse derivative terms ($\widehat{vs_y}$ in this case) are given in detail in (Almgren et al. 1998). Analogous formulae are used to predict values for $\tilde{s}^{T/B}_{i,j+1/2}$ and $\tilde{s}^{T/B}_{i,j-1/2}$ at the other cell edges.

Upwinding is used to determine $\tilde{s}$ at each edge as follows:

$$\tilde{s}_{i+\frac{1}{2},j} = \begin{cases} \tilde{s}^L_{i+\frac{1}{2},j} & \text{if } \mathrm{V}^x_{i+\frac{1}{2},j} > 0 \\ 1/2(\tilde{s}^L_{i+\frac{1}{2},j} + \tilde{s}^R_{i+\frac{1}{2},j}) & \text{if } \mathrm{V}^x_{i+\frac{1}{2},j} = 0 \\ \tilde{s}^R_{i+\frac{1}{2},j} & \text{if } \mathrm{V}^x_{i+\frac{1}{2},j} < 0 \end{cases}$$

and similarly for defining $\tilde{s}_{i,j+\frac{1}{2}}$ using V^r. Finally, we define the conservative update term,

$$[\nabla \cdot (s\mathbf{V})]^{n+1/2}_{i,j} = (\mathrm{V}^x_{i+\frac{1}{2},j}\tilde{s}_{i+\frac{1}{2},j} - \mathrm{V}^x_{i-\frac{1}{2},j}\tilde{s}_{i-\frac{1}{2},j}) + (\mathrm{V}^r_{i,j+\frac{1}{2}}\tilde{s}_{i,j+\frac{1}{2}} - \mathrm{V}^r_{i,j-\frac{1}{2}}\tilde{s}_{i,j-\frac{1}{2}}) \ .$$

The construction of $p_0{}^{n+1/2}_{j+1/2}$ and $\rho_0{}^{n+1/2}_{j+1/2}$ in **Step 3** is similar but not identical to the above procedure. Here we make no reference to $\mathbf{U}^n$. Rather

$$p_0{}^B_{j+1/2} = p_0{}^n_j + (\frac{\Delta r}{2} - w_{0j}\frac{\Delta t}{2})(p_0{}^{\lim}_r)_j$$

extrapolated from j, and

$$p_0{}^T_{j+1/2} = p_0{}^n_{j+1} - (\frac{\Delta r}{2} + w_{0j+1}\frac{\Delta t}{2})(p_0{}^{\lim}_r)_{j+1}$$

extrapolated from $j+1$. Here $w_{0j} = 1/2(w_{0j+½} + w_{0j-½})$. Upwinding then determines ${p_0}_{j+½}^{n+½}$:

$${p_0}_{j+½}^{n+½} = \begin{cases} {p_0}_{j+½}^{B} & \text{if } w_{0j+½} > 0 \\ ½({p_0}_{j+½}^{T} + {p_0}_{j+½}^{B}) & \text{if } w_{0j+½} = 0 \\ {p_0}_{j+½}^{T} & \text{if } w_{0j+½} < 0 \end{cases}$$

The evolution equation for ρ_0 differs from that for p_0 so the construction of ${\rho_0}_{j+½}^{n+½}$ differs slightly from that for ${\rho_0}_{j+½}^{n+½}$.

$${\rho_0}_{j+½}^{B} = {\rho_0}_{j}^{n} + (\frac{\Delta r}{2} - w_{0j}\frac{\Delta t}{2})({\rho_0}_{r}^{\lim})_j - \frac{\Delta t}{2}{\rho_0}_{j}^{n}(w_{0j+½} - w_{0j-½})$$

extrapolated from j, and

$${\rho_0}_{j+½}^{T} = {\rho_0}_{j+1}^{n} - (\frac{\Delta r}{2} + w_{0j+1}\frac{\Delta t}{2})({\rho_0}_{r}^{\lim})_{j+1} - \frac{\Delta t}{2}{\rho_0}_{j+1}^{n}(w_{0j+3/2} - w_{0j+½})$$

extrapolated from $j+1$. The upwinding procedure is the same.

REFERENCES

Almgren, A. 2000, Journal of Atmospheric Sciences, 57, 995

Almgren, A. S., Bell, J. B., Colella, P., Howell, L. H., & Welcome, M. L. 1998, Journal of Computational Physics, 142, 1

Almgren, A. S., Bell, J. B., & Crutchfield, W. Y. 2000, SIAM J. Sci. Comput., 22, 1139

Almgren, A. S., Bell, J. B., Rendleman, C. A., & Zingale, M. 2006, ApJ, 637, 922, paper I

Almgren, A. S., Bell, J. B., & Szymczak, W. G. 1996, SIAM J. Sci. Comput., 17, 358

Bannon, P. 1996, Journal of the Atmospheric Sciences, 53, 3606

Colella, P. 1985, SIAM J. Sci. Stat. Comput., 6, 104

—. 1990, Journal of Computational Physics, 87, 171

Colella, P., & Woodward, P. R. 1984, Journal of Computational Physics, 54, 174

Gamezo, V. N., Khokhlov, A. M., & Oran, E. S. 2005, ApJ, 623, 337

García-Senz, D., & Bravo, E. 2005, A&A, 430, 585

Glasner, S. A., Livne, E., & Truran, J. W. 2005, ApJ, 625, 347

Höflich, P., & Stein, J. 2002, Astrophysical Journal, 568, 779

Harlow, F. H., & Welch, E. 1965, Phys. Fluids, 8, 2182

Kuhlen, M. Q., Woosley, S. E., & Glatzmaier, G. A. 2006, ApJ, in press

Livne, E., Asida, S. M., & Höflich, P. 2005, ApJ, 632, 443

Niemeyer, J. C., Hillebrandt, W., & Woosley, S. E. 1996, ApJ, 471, 903

Plewa, T., Calder, A. C., & Lamb, D. Q. 2004, Astrophysical Journal, 612, L37

Röpke, F. K., & Hillebrandt, W. 2005, A&A, 431, 635

Timmes, F. X., & Swesty, F. D. 2000, ApJS, 126, 501

Woosley, S. E. 2001, Nuclear Physics A, 688, 9, Proceedings of Nuclei in the Cosmos 2000

Woosley, S. E., Wunsch, S., & Kuhlen, M. 2004, Astrophysical Journal, 607, 921

Wunsch, S., & Woosley, S. E. 2004, ApJ, 616, 1102

Zingale, M. et al. 2002, Astrophysical Journal Supplement, 143, 539

Table 1: Location of heating sources for non-uniform heating terms, Eq. 25 and Eq. 26.

i	a_i	x_i (cm)	r_i (cm)	σ_i (cm)
1	0.00625	5.0×10^7	6.5×10^7	2.5×10^6
2	0.01875	1.2×10^8	8.5×10^7	2.5×10^6
3	0.01250	2.0×10^8	7.5×10^7	2.5×10^6

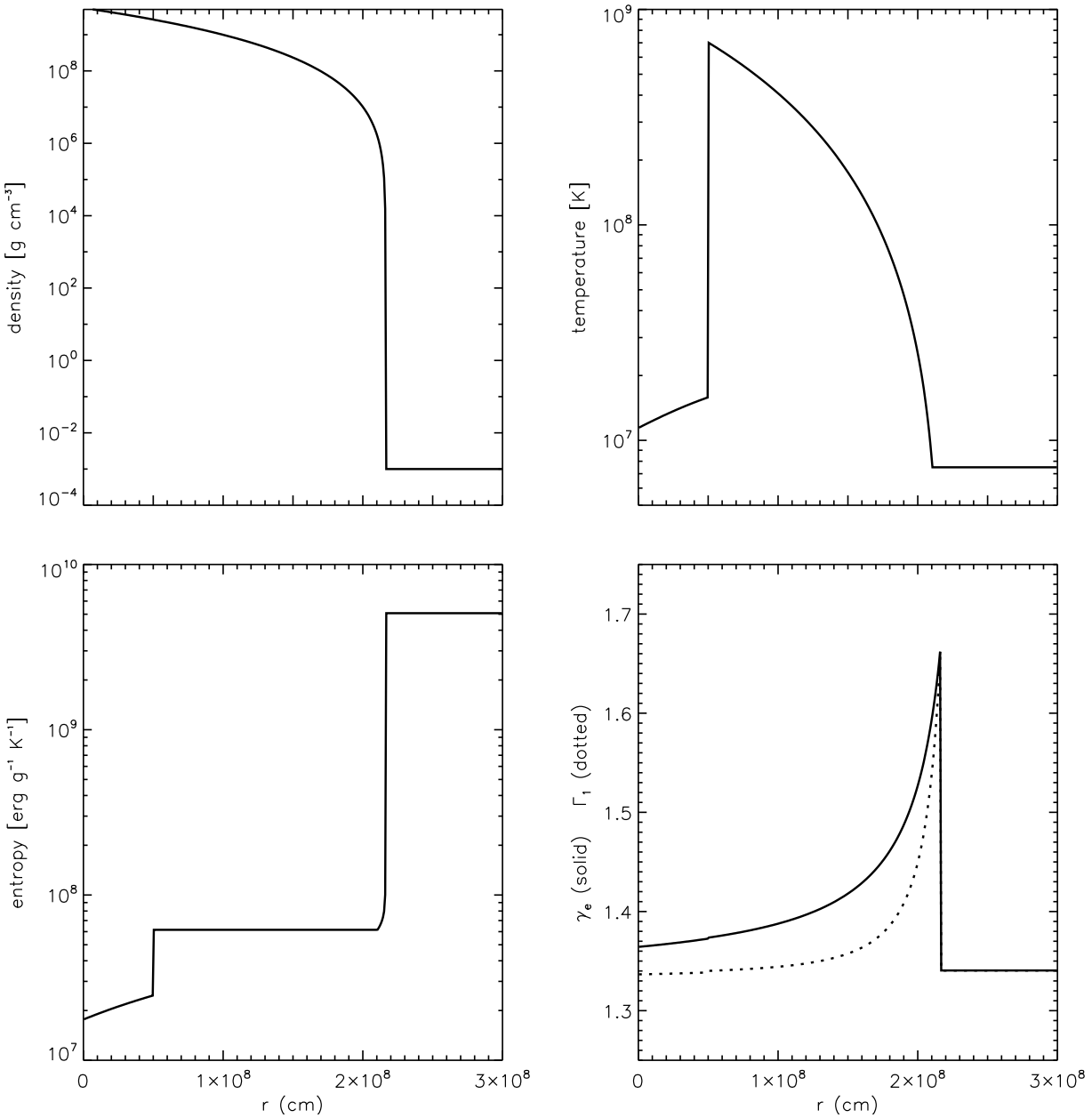

Fig. 1.— The white dwarf atmosphere initial model. Shown are the density (top left), temperature (top right), entropy (bottom left), and adiabatic indices (bottom right). To prevent convective motions from hitting the lower boundary in our multidimensional tests, the first 5×10^7 cm of this model is constructed to have a convectively stable entropy profile. The one-dimensional tests do not use this portion of the model.

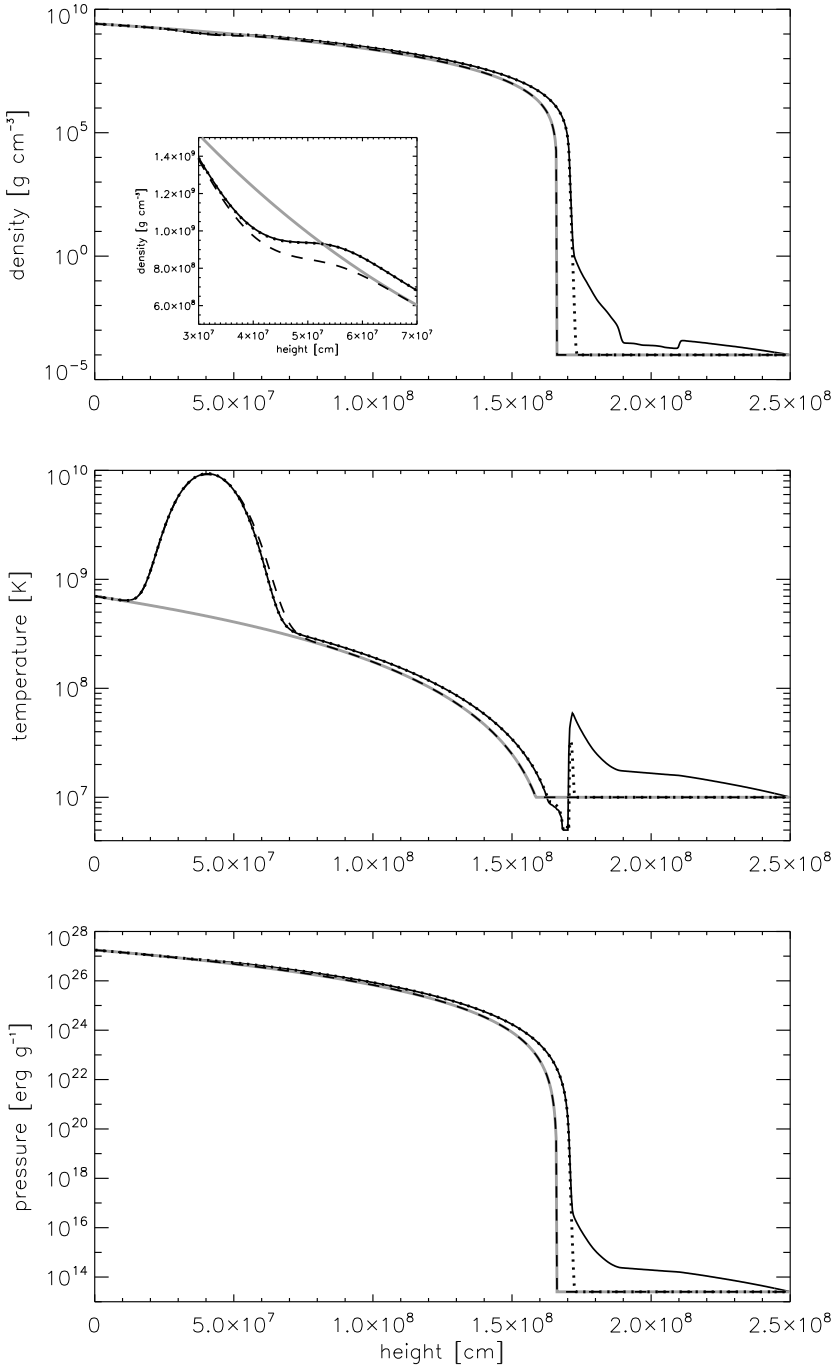

Fig. 2.— Hydrostatic adjustment problem with uniform heating: density (top), temperature (middle) and pressure (bottom). The initial conditions are shown in gray. The solid black line is the fully compressible solution, the dotted line is the low Mach number formulation that allows for the base state expansion, and the dashed line is the low Mach number formulation assuming a fixed base state. The compressible and expanding base state low Mach number solutions show excellent agreement. The low Mach number model with a fixed base state is unable to capture the correct solution. The inset in the density plot shows the structure in the vicinity of the local heating.

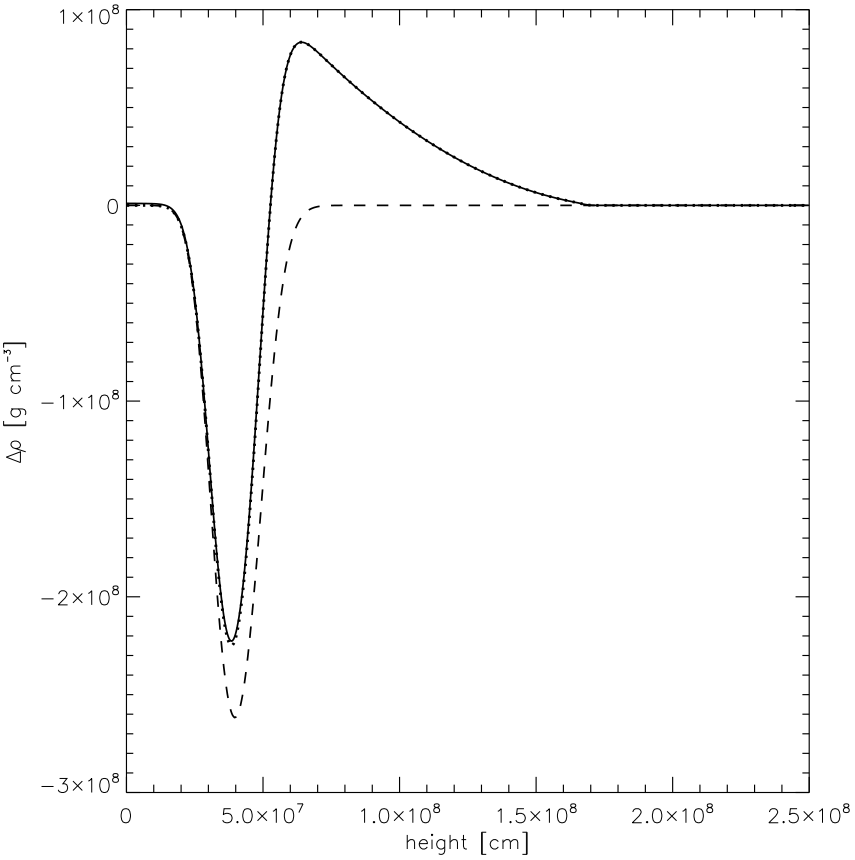

Fig. 3.— Hydrostatic adjustment problem with uniform heating: the difference in density between $t = 0$ and $t = 5$ s. The solid black line is the fully compressible solution, the dotted line is the low Mach number formulation that allows for the base state expansion, and the dashed line is the low Mach number formulation assuming a fixed base state. We see close agreement between the compressible and low Mach number formulation with the time-dependent base state.

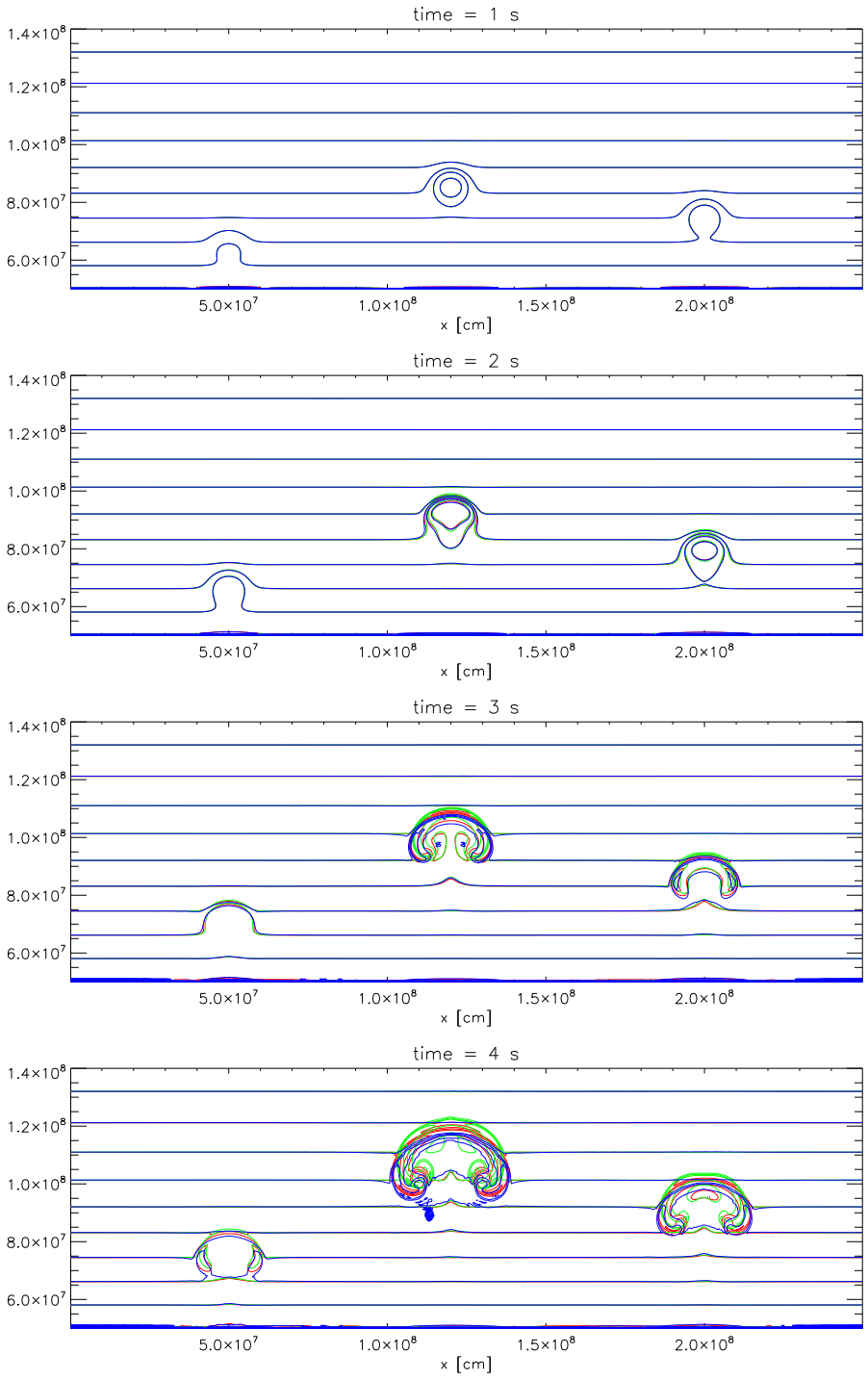

Fig. 4.— Second test case: temperature contours for the low Mach number (green), unsplit (red), and PPM (blue) solvers, shown at 1, 2, 3, and 4 s. Here, a heating source term gradually adds energy at three points in the domain (see Eq. 25) during the first 2 s of evolution. This gives rise to the three buoyant plumes seen in the panels. Contours span 10^8 K to 8×10^8 K, spaced every 5×10^7 K.

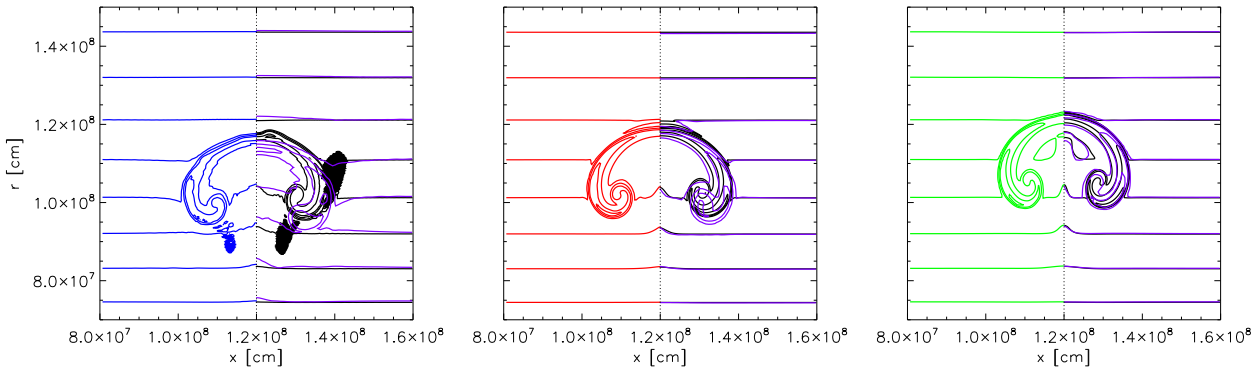

Fig. 5.— Resolution study for the second test case. Each pane shows the middle bubble from Figure 4 only; PPM results are in the left pane, unsplit results are in the middle pane, and low Mach number results are in the right pane. Within each pane, the left half is identical to the left half of the bubble in Figure 4, with the same color scheme. On the right half of each pane is a reflection around the center line of the bubble of the comparable results but at both a higher (320×448) and lower (1280×1792) resolution. The low resolution is shown in purple and the high resolution is shown in black.

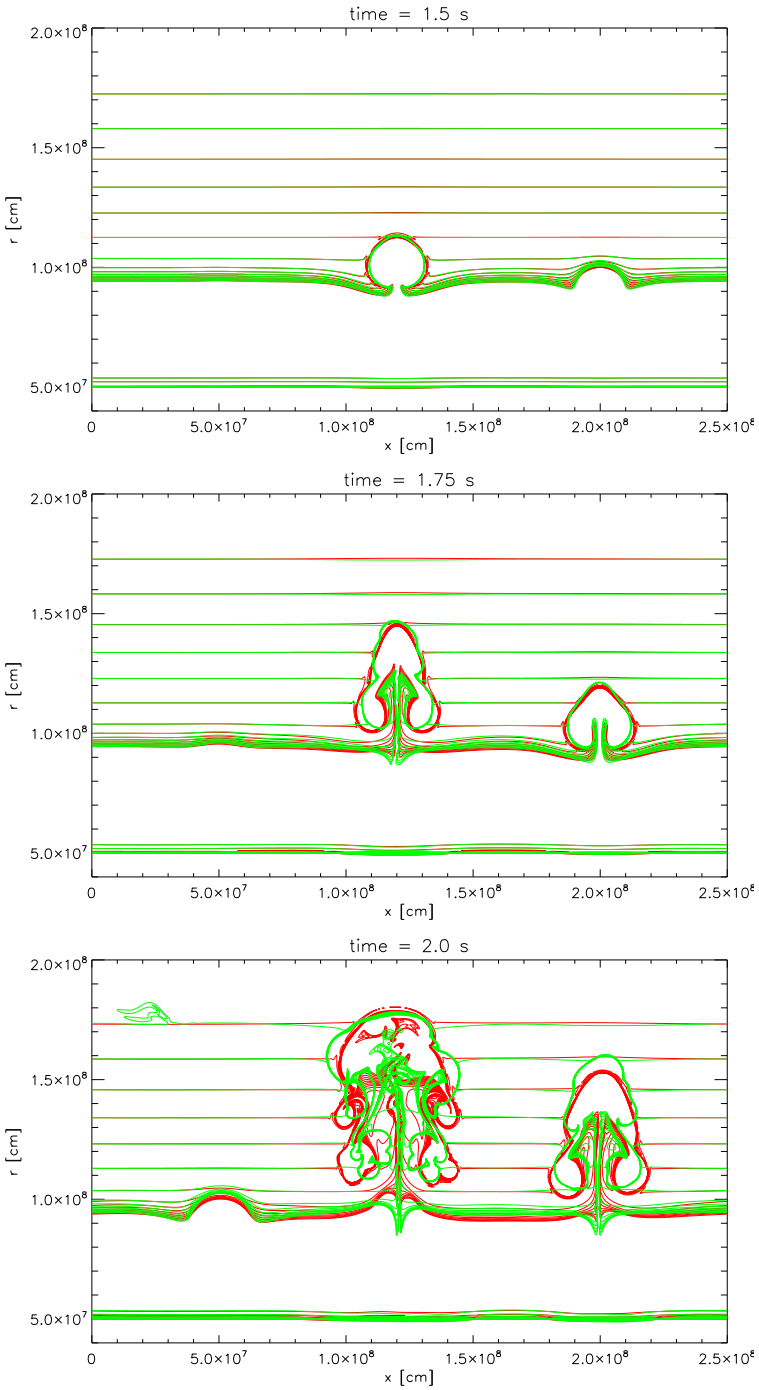

Fig. 6.— Third test case: temperature contours for the low Mach number (green) and unsplit (red) solvers. Here, in addition to the localized heating from the previous test (see Figure 4), there is a uniform heating layer centered at a height of 7.5×10^7 cm, as specified by Eq. 26. Contours span 10^8 K to 8×10^8 K, spaced every 5×10^7 K.

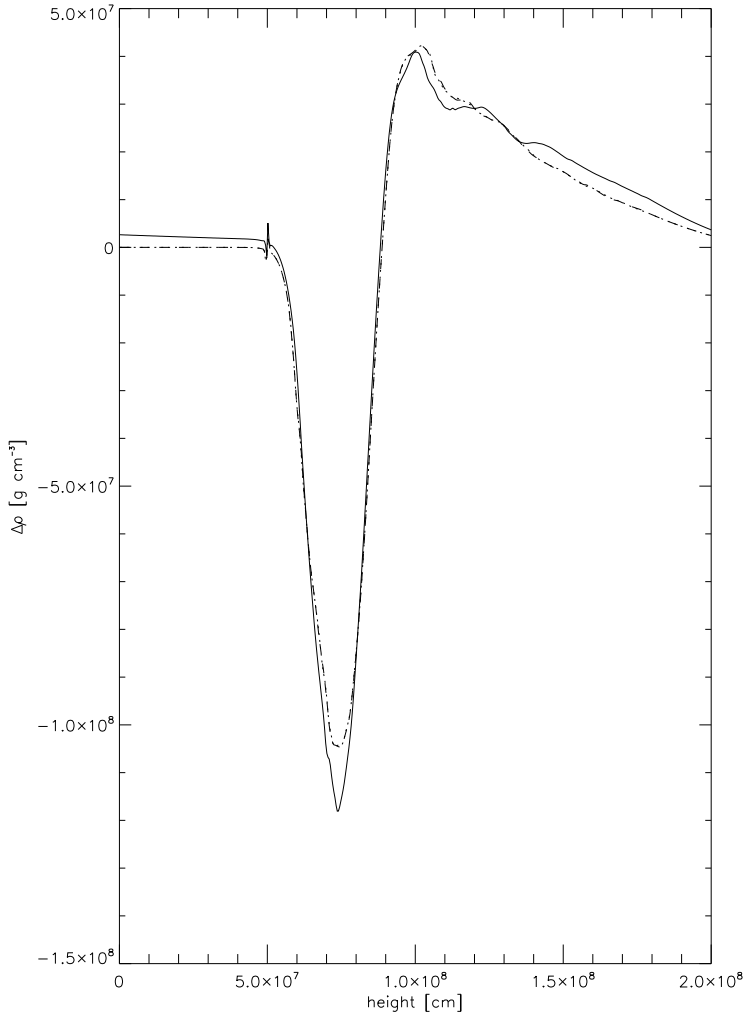

Fig. 7.— Third test case: horizontal average of the difference between density at $t = 2$ and density at $t = 0$. The dotted line shows the low Mach number results; the solid line shows results using the unsplit compressible formulation. The discrepancy between the two solutions on the left is due to the difficulties in prescribing an accurate hydrostatic lower boundary for the fully compressible calculation. Overall, however, the two algorithms agree well in the average response of the atmosphere to the heating.